Transient energy growth of optimal streaks in parallel round jets

José Ignacio Jimenez-Gonzalez, Pierre Brancher

Transient energy growth of optimal streaks in parallel round jets

J. I. Jiménez-González,[1,a)] and P. Brancher,[2]

[1]*Departamento de Ingeniería Mecánica y Minera, Universidad de Jaén, Campus de las Lagunillas, 23071 Ja én, Spain*

[2]*Institut de Mécanique des Fluides de Toulouse (IMFT), Université de Toulouse, CNRS-INPT-UPS, Toulouse, France*

We present a linear optimal perturbation analysis of streamwise invariant disturbances evolving in parallel round jets. The potential for transient energy growth of perturbations with azimuthal wavenumber $m \geq 1$ is analyzed for different values of Reynolds number Re. Two families of steady (frozen) and unsteady (diffusing) base flow velocity profiles have been used, for different aspect ratios $\alpha = R/\theta$, where R is the jet radius and θ is the shear layer momentum thickness. Optimal initial conditions correspond to infinitesimal streamwise vortices, which evolve transiently to produce axial velocity streaks, whose spatial structure and intensity depend on base flow and perturbation parameters. Their dynamics can be characterized by a maximum optimal value of the energy gain G_{opt}, reached at an optimal time τ_{opt} after which the perturbations eventually decay. Optimal energy gain and time are shown to be, respectively, proportional to Re^2 and Re, regardless of the frozen or diffusing nature of the base flow. Besides, it is found that the optimal gain scales like $G_{opt} \propto 1/m^3$ for all m except $m = 1$. This quantitative difference for azimuthal wavenumber $m = 1$ is shown to be based on the nature of transient mechanisms. For $m = 1$ perturbations, the shift-up effect [J. I. Jiménez-González *et al.*, "Modal and non-modal evolution of perturbations for parallel round jets," Phys. Fluids **27**, 044105-1–044105-19 (2015)] is active: an initial streamwise vorticity dipole induces a nearly uniform velocity flow in the jet core, which shifts the whole jet radially. By contrast, optimal perturbations with $m \geq 2$ are concentrated along the shear layer, in a way that resembles the classical lift-up mechanism in wall-shear flows. The $m = 1$ shift-up effect is more energetic than the $m \geq 2$ lift-up, but it is slower, with optimal times considerably shorter in the case of $m \geq 2$ disturbances. This suggests that these perturbations may emerge very quickly in the flow when injected as initial conditions. When the base flow diffuses, the large time scale for $m = 1$ disturbances allows the shear layer to spread and the jet core velocity to decrease substantially, thus lowering the values of corresponding optimal gain and time. For $m \geq 2$, results are less affected, since the shorter transient dynamics does not leave room for significant modifications of the base flow velocity profiles, and the scaling laws obtained in the frozen case are recovered. Nevertheless, base flow diffusion hinders the transient growth, as a consequence of a weaker component-wise non-normality and a smoother, radially spread structure of optimal disturbances.

I. INTRODUCTION

The stability of round jets has been widely studied by many authors in the past.[1–7] These studies allowed for a precise characterization of their unstable dynamics, which is dominated by the presence of co-rotating vortices generated by the Kelvin-Helmholtz instability of the shear layer between the jet flow and the fluid at rest. The existence of these structures is related, in an asymptotic or large-time framework, to the unstable nature of *modal* perturbations with particular azimuthal and axial symmetries. It is well known that the selection of the most unstable modes depends strongly on the aspect ratio of the base flow velocity profile, i.e., $\alpha = R/\theta$, where R is the jet radius and θ stands for the shear layer momentum thickness, and the Reynolds number. In general, profiles defined by low values of α are only unstable to helical perturbations (azimuthal wavenumber $m = 1$), regardless of the value of the Reynolds number,[1] although viscosity plays a stabilizing role that leads to smaller perturbation growth rates.[8] On the other hand, steeper base flow profiles, i.e., large values of α, present a wider range of unstable azimuthal wavenumbers for axially asymmetric perturbations,[2,9] including axisymmetric disturbances with $m = 0$, which become the most unstable for vanishing shear layer thickness in the inviscid limit.[7]

This stability scenario for jets may be, however, modified if other types of short time unstable dynamics are activated. In that sense, shear flows are also known to sustain large algebraic energy growth,[10] where a particular disturbance, asymptotically stable or not in the long time limit, may be amplified transiently by means of specific physical mechanisms. This transient growth is related to inviscid instabilities whereby shear flows can be unstable to disturbances in the cross-stream velocity components, whose kinetic energy grows linearly in time, even though the base flow does not contain any inflection point.[11,12] For the particular case of round jets, recent works

on non-modal instability[13,14] have shown that transient growth of helical perturbations (azimuthal wavenumber $m = 1$) is favored by this algebraic instability, due mainly to the *lift-up* effect,[11,12,15] although the Orr mechanism,[16] i.e., the progressive vortex sheet alignment with shear, has been also proven to occur in jets subjected to optimal harmonic forcing.[17] In an attempt to unravel the role of different transient mechanisms in round jets, Jiménez-González *et al.*[18] have recently identified two mechanisms, within the framework of a parametric study aiming at analyzing the influence of the jet velocity profile on the instability of axisymmetric ($m = 0$) and helical ($m = 1$) perturbations. More precisely, it has been found that an Orr-type mechanism is responsible for the energy gain of helical and axisymmetric disturbances of small axial wavelength, whereas a specific mechanism, the so-called *shift-up* effect which shifts the jet as a whole, is found to cause transient growth for $m = 1$ helical disturbances with long axial wavelength, in a way that resembles the classical lift-up effect. This mechanism provides with the largest energy gain for vanishing perturbations axial wavenumbers, by generating intense streamwise velocity streaks induced by streamwise counter-rotating vortices. Consequently, the shift-up effect is expected to be particularly efficient in the limit of streamwise invariant disturbances (axial wavenumber $k = 0$), when the vortex structures are aligned with the axial direction.

If the transient amplification of kinetic energy for axially invariant perturbations is sufficiently large, in view of previous results on shear flows,[15] it could be conjectured that a nonlinear transition may be eventually triggered in the jet, when the perturbation is initially injected, which might be used to control unstable asymptotic disturbances. For instance, the generation of Kelvin-Helmholtz vortex rings and its subsequent subharmonic instability leading to the merging of vortices in pairs, i.e., vortex pairing,[19] is a source of aeroacoustic noise which is important to control or even suppress in many industrial applications because of noise nuisance or acoustic stealth. In that sense, several studies have recently dealt with active and passive strategies to control coherent structures in jets, enhance mixing, and reduce noise, both in laminar and turbulent regimes. For instance, New and Tay[20] demonstrated, for a laminar round jet (Reynolds number below 2500), that streamwise counterrotating vortex pairs, generated by means of radial control jets, may contribute to noise suppression by enhancing the turbulent mixing and the breaking-down of shear layer rolls, which become increasingly less coherent as the mass ratio of control jets is increased. Besides, Alkislar *et al.*[21] investigated the effect of chevrons and microjets on the acoustic field of a jet with Mach number 0.9, showing that the emergence of streamwise vortex pairs, lying on the high speed zone of the initial shear layer, provides with a relatively uniform noise reduction for a wide range of sound radiation angles. Similarly, Zhang[22] identified, for a turbulent round jet, an overall low-frequency noise reduction when an active control based on unsteady radial microjets was applied. Interestingly, these initial jets may evolve into coherent azimuthally fixed streamwise vortices that enhanced turbulent boosting and mixing, as shown by Yang *et al.*[23]

In view of previous results, one possible approach to reduce noise and enhance mixing consists in actually canceling the Kelvin-Helmholtz vortices that are directly involved in the pairing phenomenon and the noise generation, by means of streamwise vortices fostering. For this purpose, the former conjecture may be used to inject an *optimal* perturbation at the jet exit, with the aim at triggering transiently an instability which differs from the Kelvin-Helmholtz vortex rings. Thus, an eventual nonlinear saturation of this specific instability could lead to a new structure of the jet flow that could be robust with respect to the Kelvin-Helmholtz instability, bypassing then the formation of vortex rings and their subsequent pairing and the generation of aeroacoustic noise, although such scenario might be strongly dependent on the initial amplitude of the injected optimal perturbation and corresponding energy gain, and the competition between time scales in which transient growth and modal instabilities develops (see, e.g., the work of Bakas and Ioannou[24]). In any case, although there is no guarantee that such strategy succeeds, the application of optimal disturbances to the control of flows has been satisfactorily applied to different unstable shear flows. For instance, Cossu and Brandt[25,26] have shown that optimal perturbations in the form of streamwise counter-rotating vortices, which transiently evolves towards periodic streamwise streaks through the inviscid lift-up effect,[12] leads to three-dimensional modulations of the Blasius boundary layer profile, which renders the flow more robust with respect to the Tollmien-Schlichting instability. A similar observation has been recently made for two-dimensional wakes by Del Guercio *et al.*,[27–29] where the optimal transient amplification of linearly stable streamwise vortices leads to the global stabilization of the von Kármán vortex street. Similar results have been recently obtained for three-dimensional axisymmetric wakes,[30] using steady optimal disturbances. The common nature of optimal disturbances and the transient growth mechanism for different shear flows is also evidenced by the scaling laws governing the dynamics. The optimal energy gain scales with the square of the Reynolds number, for two-dimensional wakes[27] and boundary layers,[25] in line with the analysis for the plane Poiseuille flow carried out by Gustavsson.[31] In view of results of recent studies on non-modal stability of round jets,[14,18] where transient dynamics leads to energetic amplification of the streamwise velocity component, especially in the limit $k/m \longrightarrow 0$, it is expected that the strategies implemented for the stabilization of boundary layers and wakes could be used with a comparable efficiency for jet flows. Particularly relevant are results on the control of globally unstable wakes[28,30] by means steady optimal perturbations, since for these studies, the absolute modal instability, giving rise to the von Kármán street, was fully established before the injection of any optimal initial streamwise vortex. Thus, it is shown that if the initial amplitude of optimal disturbances exceeds a critical threshold, the nonlinear flow saturation might induce the weakening of the absolute instability. That may suggest that efficient bypass solutions can be achieved when the transient energy gain of perturbation overcomes the most unstable modal energy gain, even though slower time scales may characterize the optimal perturbation growth. Besides, the application of hydrodynamic and algebraic instability analyses to control jet break-up in engines[32,33] has been also based on the experimental observations of streamwise ligaments and other streamwise patterns in

jet flows,[34] which suggests that the use of the non-modal disturbances may actually provide a satisfactory characterization of jet control problems.

Prior to the application of any control strategy, a complete analysis of the potential for the transient growth of streamwise invariant perturbations is required in parallel round jets of different velocity profiles and different Reynolds numbers. As mentioned earlier, three-dimensional optimal perturbations are shown to be most efficient in the control of shear flows, so the analysis will focus only on optimal disturbances with azimuthal wavenumbers $m \geq 1$. In that context, the shift-up mechanism, characterized by a radial displacement and the subsequent emergence of streamwise velocity streaks in the jet core, has been shown to take place for $m = 1$, but it still remains to study whether disturbances with higher azimuthal wavenumbers undergo also large transient energy growth and to characterize the transient mechanism at play and its link with the lift-up effect, which is expected to act inside the shear layer. More precisely, the present study, which may be considered as a initial step on the control methodology for Kelvin-Helmholtz instabilities, aims at unveiling the transient mechanisms and characterizing the influence of some flow parameters, such as the jet aspect ratio, the Reynolds number, and the perturbation azimuthal symmetry, on the optimal energy gain and time of streamwise invariant disturbances.

The paper is organized as follows: the problem formulation and technical aspects are presented in Sec. II. Optimal perturbation results are presented in Sec. III, where the effect of using steady or unsteady (diffusing) base flow velocity profiles is investigated in Secs. III A and III B, respectively. The paper ends with the conclusions and perspectives in Sec. IV.

II. PROBLEM FORMULATION AND TECHNICAL BACKGROUND

A. Base flow

Two families of base flows, consisting in steady or unsteady axisymmetric parallel jets, have been investigated. The first family corresponds to steady base flows that stem from the classical profile proposed by Michalke,[35] whose velocity distribution can be expressed in cylindrical coordinates (r, ϕ, z) as $\mathbf{U} = U(r)\,\mathbf{e}_z$. Using as characteristic scales the jet centerline velocity U_j and the jet radius R, at which the axial velocity is $U = U_j/2$, the Reynolds number is defined s $Re = \rho U_j R/\mu$, where ρ and μ are, respectively, the fluid density and kinematic viscosity. The non-dimensional base flow velocity profile reads

$$U(r) = \frac{1}{2}\left\{1 + \tanh\left[\frac{\alpha}{4}\left(\frac{1}{r} - r\right)\right]\right\}, \tag{1}$$

with $\alpha = R/\theta$ the ratio between the jet radius R and the shear layer momentum thickness θ. The latter is defined, using dimensional variables $\tilde{r}$ and $\tilde{U}$, as

$$\theta = \int_0^\infty \left[1 - \tilde{U}(\tilde{r})/U_j\right] \tilde{U}(\tilde{r})/U_j \, d\tilde{r}. \tag{2}$$

A characteristic Michalke's velocity profile with aspect ratio $\alpha = 50$ can be observed in Fig. 1(a) (dotted line). This type of velocity profile will be considered in the first part of the optimal perturbation analysis as steady (frozen) base flows.

However, the use of a frozen velocity profile may represent a strong assumption for cases in which the transient dynamics of perturbation is characterized by long optimal times. That would give the base flow enough time to diffuse and modify the transient growth scenario, therefore leading to inadequate results in the frozen framework. In that context, the optimal perturbation analysis has been extended to a second family of base flows that correspond to diffusing jet velocity profiles $U(r, t)$, which will allow us to evaluate the validity and limitations of the classical frozen analysis. This family of velocity profiles is built on the analytical solution of the viscous diffusion of the top-hat jet (i.e., initially uniform velocity jet profile). The initial base flow profiles considered in this second part of the study then correspond to the solution of the diffusing top-hat jet at some given time, after non-dimensionalization to have unit velocity on the axis and unit jet radius where the velocity is half the maximum velocity, i.e., $U(r = 1, t = 0) = 0.5$. The derivation and computation of the diffusing base flow are detailed in Appendix A. Velocity profiles at initial time are characterized by the aspect ratio α, whose influence on $U(r, t = 0)$ is shown in Fig. 1(a). Interestingly, it is observed that in the limit of high α, e.g., 50, the diffusing velocity profile coincides with Michalke's profile [see the dotted line in Fig. 1(a)], indicating that both families of base flows are equivalent for large shear (top-hat) profiles. Similarly, in the limit of the vanishing shear layer, at low values of α, e.g., 3.3, the velocity profile corresponds to the classical Gaussian jet [dashed line in Fig. 1(a)]. The latter can be analytically derived from Eq. (A7), which gives the temporal evolution of diffusing base flows.

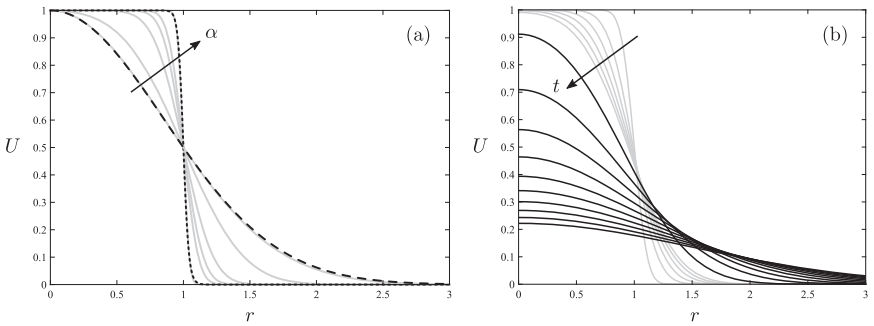

FIG. 1. (a) Initial diffusing base flow velocity profiles for $\alpha = 3.3$, 5, 10, 15, 20, and 50. The profiles at $\alpha = 50$ and $\alpha = 3.3$ are, respectively, indistinguishable from Michalke tanh profile (dotted line) and a Gaussian profile (dashed line). (b) Time evolution of the base flow velocity profile with initial $\alpha = 20$, for t/Re from 0 to 0.05 in increments of 0.01 (gray lines) and from 0.1 to 1 in increments of 0.1 (black lines).

As an instance, Fig. 1(b) displays the temporal diffusion of a velocity profile with initial $\alpha = 20$, for different times, which are scaled with Re.

The optimal perturbation analysis with this parametric diffusing base flows will be limited to initial aspect ratios of $\alpha \geq 5$. However, results corresponding to lower values of α are included in Appendix C, *via* the use of a diffusing Gaussian velocity profile.

B. Optimal perturbation analysis

As mentioned earlier, energetic transient growth mechanisms of perturbations might lead to a nonlinear flow transition in jets. The potential risk for such a by-pass scenario can be evaluated by the quantification of transient amplification of kinetic energy of disturbances. For this purpose, we perform an optimal perturbation analysis for specific streamwise invariant perturbations, where we study the temporal evolution of infinitesimal disturbances of the base flow, $\mathbf{q}' = (\mathbf{u}', p')$, with velocity $\mathbf{u}' = (u'_r, u'_\phi, u'_z)$ and pressure p'. Assuming a classical normal mode decomposition in the azimuthal direction and considering the streamwise flow invariance, it yields $\mathbf{q}'(r, \theta, t) = [\mathbf{u}(r, t), p(r, t)] \exp[i(m\phi)] + c.c.$, where $\mathbf{u} = (u_r, u_\phi, u_z)$ and p correspond, respectively, to the velocity and pressure amplitudes, m (integer) is the azimuthal wavenumber, and $c.c.$ denotes the complex conjugate. Linearizing the Navier-Stokes equations around the base flow (which are made non-dimensional using, respectively, R, U_j, R/U_j, and ρU_j^2, as characteristic length, velocity, time, and pressure scales) and expressing p and u_θ as functions of u_r and u_z, we obtain a compact system in terms of $\mathbf{v} = (u_r, u_z)^T$,

$$F(\mathbf{v}) = L\frac{\partial \mathbf{v}}{\partial t} + C\mathbf{v} - \frac{1}{Re}D\mathbf{v} = 0, \tag{3}$$

L, C, and D being linear operators, defined as follows:

$$L = \begin{pmatrix} r^2\frac{\partial^2}{\partial r^2} + 3r\frac{\partial}{\partial r} - (m^2 - 1) & 0 \\ 0 & -1 \end{pmatrix},$$

$$C = \begin{pmatrix} 0 & 0 \\ -\frac{\partial U}{\partial r} & 0 \end{pmatrix},$$

$$D = \begin{pmatrix} r^2\frac{\partial^4}{\partial r^4} + 6r\frac{\partial^3}{\partial r^3} - (2m^2 - 5)\frac{\partial^2}{\partial r^2} - \frac{2m^2+1}{r}\frac{\partial}{\partial r} + \frac{(m^2-1)^2}{r^2} & 0 \\ 0 & -\frac{1}{r}\frac{\partial}{\partial r}\left(r\frac{\partial}{\partial r}\right) + \frac{m^2}{r^2} \end{pmatrix}, \tag{4}$$

which include spatial derivatives of perturbations and base flow, where U corresponds to the base flow profile considered in the analysis, i.e., either frozen, $U(r)$, or diffusing, $U(r, t)$. The problem formulation is closed with the appropriate boundary conditions for the perturbations, namely, decay at infinity and regularity at the origin, which is defined by the essential *pole conditions*[1] at the axis, which state that any perturbation field is independent of the azimuthal coordinate, ϕ, at $r = 0$. The initial value problem defined by Eq. (3) can be solved to obtain the temporal evolution of disturbances. Instead of looking for unstable perturbations at asymptotic temporal horizons, as done in a classical modal temporal analysis, we are interested in the short time transient dynamics, with the aim at evaluating the potential for nonlinear flow distortion as a strategy to control shear instability.[27] Therefore, we compute optimal perturbations for finite time horizons, i.e., the initial conditions that maximize the gain of energy during a finite time interval $[0, \tau]$, where the gain defined as the ratio between the perturbation kinetic energy density at the final time $t = \tau$ and that at the initial time $t = 0$,

$$G(\tau) = \frac{E(\tau)}{E(0)}, \tag{5}$$

with

$$E(t) = \frac{1}{2}\int_0^\infty \left(|u_r(r,t)|^2 + |u_\phi(r,t)|^2 + |u_z(r,t)|^2\right) r\, dr, \tag{6}$$

which represents the energy per unit length in z and unit angle in ϕ. To solve the optimization problem, we adopt the formalism introduced by Corbett and Bottaro,[36] which consists in maximizing the energy gain $G(\tau)$, constrained by the linearized system of Eq. (3) and the associated boundary conditions, using the perturbation at initial time $t = 0$ as the control variable. The problem can be tackled by introducing the unconstrained Lagrangian functional

$$\mathcal{L}(\mathbf{v}, \mathbf{v_0}, \mathbf{a}, \mathbf{c}) = G(\tau) - \langle F(\mathbf{v}), \mathbf{a} \rangle - (H(\mathbf{v}, \mathbf{v_0}), \mathbf{c}), \tag{7}$$

where $\mathbf{a}(r, t)$ and $\mathbf{c}(r)$ are the adjoint (or co-state) variables that work as Lagrange multipliers. The last term imposes the initial condition, which must match the control condition, $H(\mathbf{v}, \mathbf{v_0}) = \mathbf{v}(0) - \mathbf{v_0} = 0$. Besides, the inner products appearing at the functional are, respectively,

$$(H(\mathbf{v}, \mathbf{v_0}), \mathbf{c}) = \int_{\mathbf{0}}^{\infty} \overline{H(\mathbf{v}, \mathbf{v_0})} \cdot \mathbf{c}\; rdr + c.c. \tag{8}$$

and

$$\langle F(\mathbf{v}), \mathbf{a} \rangle = \int_0^\tau \int_0^\infty \overline{F(\mathbf{v})} \cdot \mathbf{a}\; rdrdt, \tag{9}$$

where overbars denote transconjugate. The problem reduces to find the set of variables $(\mathbf{v}, \mathbf{v_0}, \mathbf{a}, \mathbf{c})$ corresponding to a stationary Lagrangian functional, $\mathcal{L}$, by setting to zero the directional derivative with respect to an arbitrary variation in the set of variables (see the work of Corbett and Bottaro[36] for further details). This step provides with transfer relations between direct and adjoint variables at $t = \tau$ and $t = 0$, which is employed to obtained the optimal perturbation, $\mathbf{v_0} = \frac{1}{2}(E(0)^2/E(\tau))\mathbf{a}(0)$, and the adjoint system for the co-state variable $\mathbf{a}$ that reads

$$F(\mathbf{a}) = -L\frac{\partial \mathbf{a}}{\partial t} + C^+\mathbf{a} - \frac{1}{Re}D\mathbf{a} = 0, \tag{10}$$

where C^+ is the adjoint operator of C, i.e., its transpose. The strategy followed[37,38] ensures a quick convergence after a few

iterations, starting from any initial condition. The algorithm integrates the direct system first from $t = 0$ to $t = \tau$, followed by an integration of the adjoint system backwards in time, after applying the transfer condition. When the diffusing base flow, $U(r, t)$, is considered, Eq. (A7) must be accordingly solved for each instant t considered in the integration time span. Once the iteration is completed, the initial condition $\mathbf{v_0}$ provides a new guess to start again the loop. The process stops when variations of $G(\tau)$ are below 10^{-2}, providing then with the converged optimal perturbation $\mathbf{v_0}$.

C. Numerical aspects

We employ the same numerical method as in previous studies,[18] where technical and convergence issues are detailed. In short, the derivatives are computed with a pseudospectral method,[39] which uses a Gauss-Lobatto grid that is adjusted into a semi-infinite domain through an algebraic mapping.[40] Grid and differentiation matrices are computed using MATLAB and the DMSuite package,[41] considering parity properties of functions in the expression of derivatives,[42] to ensure regularity and smoothness of solution near the axis. More precisely, in order to avoid the geometric singularity at the axis $r = 0$ and to force the regularity of the solution in its neighbourhood, parity properties of functions with azimuthal dependence of the form $\exp(im\phi)$ have been used, ensuring the smoothness of the solution near the axis.[42] These conditions are based on the representation in cylindrical coordinates and the fact that $\exp(im\phi)$ functions are therefore radially even or uneven, being invariant under the transformation: $\mathcal{F} : (r, \phi, z) \longrightarrow (-r, \phi \pm \pi, z)$. Hence, parity conditions read as

$$p(-r, z) = (-1)^m p(r, z), \tag{11}$$

$$u_r(-r, z) = -(-1)^m u_r(r, z), \tag{12}$$

$$u_\phi(-r, z) = -(-1)^m u_\phi(r, z), \tag{13}$$

$$u_z(-r, z) = +(-1)^m u_z(r, z). \tag{14}$$

Thus, by imposing such radial parities, the correct axial behaviour is implicitly established, without having to state explicitly the mentioned pole conditions.[1] Besides, the computations can be reduced to half the domain, $r > 0$, as commented in Appendix D, which also includes the numerical convergence analysis performed to ensure validity and robustness of results, focusing especially at largest values of Re and α, to rule out possible unstable effects of inviscid flow and steepest base flow profiles.

III. RESULTS AND DISCUSSION

A. Non-diffusing base flow

We first present results concerning the optimal perturbation analysis for the frozen base flow defined in Eq. (1). Figure 2(a) displays curves of transient optimal energy gain $G(\tau)$ as a function of the final time τ for $m = 1$ perturbations, at $Re = 1000$, and for different jet aspect ratios, ranging from $\alpha = 4$ to 40 (the arrow indicates growing α). For each curve, a global optimal gain, $G_{opt}(\alpha, m, Re) = \sup_\tau G(\tau, \alpha, m, Re)$, is reached at a specific temporal horizon τ_{opt}, after which the transient amplification decays monotonically towards zero at large times. Evolutions of G_{opt} and τ_{opt} with the aspect ratio α are displayed, respectively, in Figs. 2(b) and 2(c), where optimal perturbations at $m = 2$ are also included (larger azimuthal wavenumbers do not undergo transient growth at $Re = 1000$, and therefore they are not shown). For the range of α considered here, the maximum optimal gain slightly grows as the jet velocity profile steepens (growing α), until it reaches an asymptotic value which depends on the azimuthal wavenumber m. Note that transient amplification of $m = 1$ perturbations provides optimal energy gains which are four orders of magnitude larger than those of $m = 2$, suggesting that the transient mechanism is much more efficient in the first case. Optimal times τ_{opt} slightly decrease with α, with a shorter transient dynamics for optimal perturbations at $m = 2$ compared to $m = 1$.

The influence of the Reynolds number on the transient growth process is illustrated in Figs. 3(a) and 3(b), where results of the optimal perturbation analysis are presented for $Re = 10\,000$. First, we observe that a larger number of azimuthal wavenumbers ($m = 1, 2, \ldots, 6$) lead to transient growth, as a consequence of the destabilizing effect of a larger Re. A similar observation has been made for optimal energy growth in the Hagen-Poiseuille flow,[43] for which the critical Reynolds number Re_{cr}, below which there is no growth, increases with the azimuthal wavenumber m. $G_{opt}(\alpha)$ and $\tau_{opt}(\alpha)$ display trends similar to those depicted in Fig. 2 at lower Re, but larger global gains are reached at larger optimal times, similarly to what occurs for other wall-bounded[10] and unbounded shear flows,[27] For a given value of Re, asymptotic values of G_{opt} are reached for larger values of α as m increases [Fig. 3(a)], which might suggest that a thinner shear layer thickness is required for the transient growth mechanism to adapt to a shorter azimuthal disturbance wavelength and to optimally transfer energy from the jet to the perturbation (the same kind of behaviour is observed in multiphase jets[14] where the

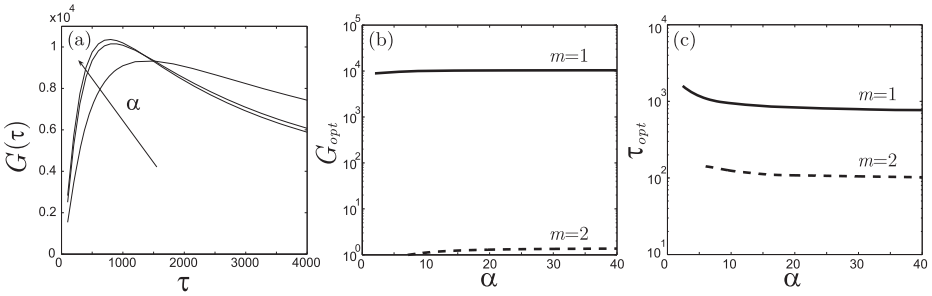

FIG. 2. Frozen base flow at $Re = 1000$: (a) energy gain $G(\tau)$ for $m = 1$ and different values of $\alpha \in [4, 12, 40]$, (b) global optimal gain $G_{opt}(\alpha, m)$, (c) optimal time $\tau_{opt}(\alpha, m)$ for $m = 1, 2$. The arrow indicates increasing values of α.

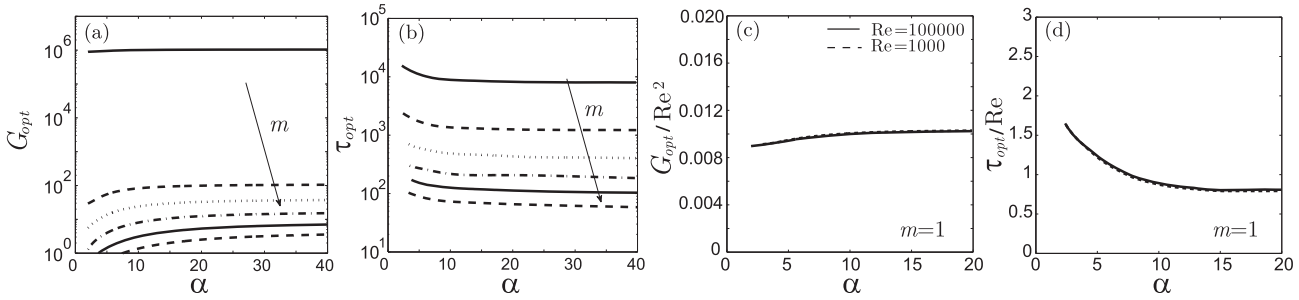

FIG. 3. Frozen base flow: dependence on α of maximum optimal growth $G_{\max}$ (a) and optimal time τ_{opt} (b) at $Re = 10\,000$ (arrows indicate growing values of m, i.e., $1, 2, \ldots, 6$). Rescaled global optimal gain G_{opt}/Re^2 (c) and optimal time τ_{opt}/Re (d) for $m = 1$ disturbances at two different Reynolds numbers.

azimuthal wavelength of amplified disturbances is proportional to the thickness of the vorticity layer of surrounding air).

G_{opt} and τ_{opt} are found to scale, respectively, with Re^2 and Re for all values of α, as evidenced in Figs. 3(c) and 3(d), where the rescaled global optimal gain G_{opt}/Re^2 and optimal time τ_{opt}/Re are only displayed for $m = 1$ although the same Re-dependence applies for larger azimuthal wavenumbers m, with lower values. This influence of m is illustrated in Figs. 4(a) and 4(b), which displays the rescaled optimal gain G_{opt}/Re^2 and optimal time τ_{opt}/Re, for different values of m at $\alpha = 20$. The rescaled optimal gains and times for different Re collapse for each value of m and decrease monotonously for larger m (in agreement with previous results on optimal perturbation for a circular pipe flow[43]). Note that for $Re = 100\,000$, transient growth is active for perturbations with azimuthal wavenumbers up to $m = 16$, although Fig. 4 includes only results for $m \leq 7$ for the sake of clarity at low values of m. It is noteworthy that both G_{opt}/Re^2 and τ_{opt}/Re decrease monotonously for $m \geq 2$ while the case $m = 1$ is offset from this trend. This observation might indicate that the mechanism governing the transient amplification of $m = 1$ perturbations differs from the one at play for larger values of m.

The specificity of the $m = 1$ optimal perturbation is confirmed in Fig. 4(c), which displays the azimuthal distribution of the optimal perturbation radial velocity in the jet shear layer (at $r = 1$) for different values of m. It is found that for a given kinetic energy, the azimuthal wavenumber that leads to the largest values of radial velocity in the jet shear layer is $m = 1$, the values for higher m being more than one order of magnitude lower. Since the source term of kinetic energy production is related to $-u_r dU/dr$, it is then expected that the $m = 1$ optimal perturbation will benefit, in a privileged way, from the large levels of radial velocities u_r where the shear dU/dr is extremum, i.e., within the jet shear layer.

In order to gain further insight in the growth mechanism, we present in Fig. 5 the transient dynamics of optimal $m = 1$ and $m = 2$ perturbations at $Re = 1000$ for a base flow velocity profile with $\alpha = 20$. In particular, contours of axial vorticity ω_z and velocity vectors of the optimal initial conditions [Figs. 5(b) and 5(d)] and contours of axial velocity u_z of the optimally amplified disturbances at $t = \tau_{opt}$ [Figs. 5(c) and 5(e)] are displayed in a cross-sectional plane perpendicular to the axial direction. Optimal initial conditions correspond to streamwise counter-rotating vortices that are associated with a velocity field that is maximum between the structures. More precisely, for the $m = 1$ optimal perturbation, the shift-up effect[18] is observed, whereby two axial vortices form a dipole that extends over the whole jet section [see Fig. 5(b) and the white dashed lines that mark the boundaries of the shear layer]. The velocity field induced by this large scale dipole turns out to be a nearly uniform flow in the jet core. This flow leads to a global, quasi-solid-body translation of the jet radially, thus creating, at optimal time $t = \tau_{opt}$, an increase (respectively, decrease) of axial perturbation velocity on the side (respectively, opposite side) where the induced cross-sectional flow points [see Fig. 5(c)]. It should be noted that only perturbations with azimuthal wavenumber $m = 1$ induce non-zero radial velocity at the center of the jet, while higher values of azimuthal wavenumber barely perturb the jet core.

This is confirmed for the optimal $m = 2$ perturbation, as Fig. 5(d) shows. Now the optimal initial streamwise vortices are more concentrated along the shear layer and feature low vorticity magnitude [see values of ω_z in Fig. 5(b) for comparison]. This vorticity distribution leads to a cross-sectional velocity field which is negligible at the jet core. Therefore the

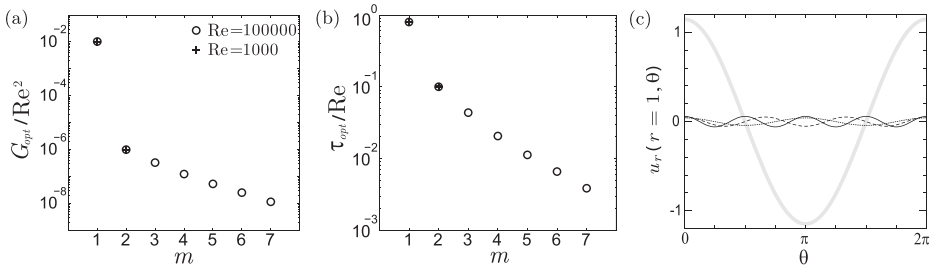

FIG. 4. Frozen base flow ($\alpha = 20$): dependence on m of (a) G_{opt}/Re^2 and (b) τ_{opt}/Re and (c) azimuthal distribution of the optimal perturbation radial velocity in the jet shear layer (at $r = 1$) for $Re = 10\,000$ and $m = 1$ (bold gray curve), $m = 2$ (dotted line), $m = 3$ (dashed line), $m = 4$ (solid line).

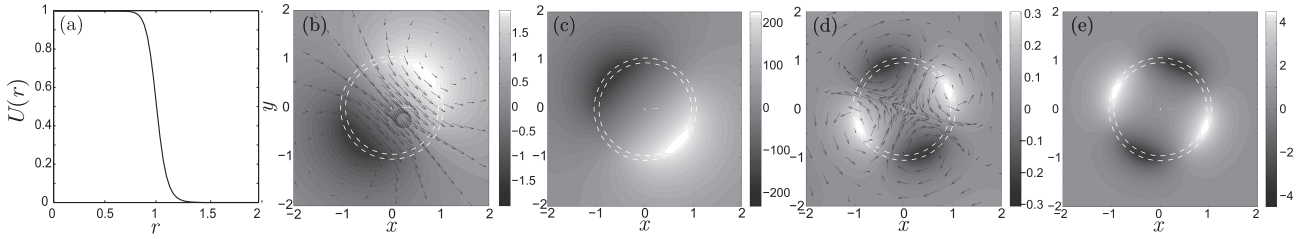

FIG. 5. Transient dynamics of perturbations for a frozen base flow with $\alpha = 20$ and $Re = 1000$: cross section of the optimal initial condition ($t = 0$) axial vorticity ω_z and associated normalized vector field [(b) and (d)] and streamwise velocity u_z of the corresponding optimally amplified ($t = \tau_{opt}$) streak [(c) and (e)], for $m = 1$ [(b) and (c)] and $m = 2$ perturbations [(d) and (e)]. Dashed circles in (b)-(e) mark the limit of the shear layer, i.e., $r = 1 \pm 1/\alpha$. Base flow velocity profile $U(r)$ is also depicted in (a).

response of the flow will be different from the global shift-up effect observed in the $m = 1$ case. As already evidenced in Fig. 4(c), the magnitude of the radial velocity perturbation u_r is lower than that induced by the $m = 1$ optimal disturbance, and consequently, a weaker energy gain is expected. This is illustrated by Fig. 5(e), where the optimally amplified streaks at $t = \tau_{opt}$ are shown to feature velocities that are two orders of magnitude lower than those displayed in Fig. 5(c). As occurs in other shear flows[44] where the classical lift-up effect is involved, streaks are located close to regions of largest mean shear $dU(r)/dr$, since for the inviscid limit, temporal growth of perturbation axial velocity is known to follow the relation: $\partial u_z/\partial t \propto u_r dU(r)/dr$. Hence, the transient lift-up mechanism will become, in principle, less efficient as the radial component of the optimal initial condition u_r is lower. In that context, the shift-up mechanism can be therefore considered a particular energetic version of the classical lift-up, for which the $m = 1$ symmetry of the optimal perturbation allows to maximize the radial velocity in the jet shear layer at initial time, which results in a nearly uniform flow in the jet core that affects the entire flow, and not only the shear layer as for $m \geq 2$, by shifting the jet as a whole. Besides the fact that the particularly high levels of radial velocities in the jet shear layer for $m = 1$ foster the energy growth, it should be noted that, in the case of a free jet, the spatial extension of the $m = 1$ dipole is not constrained and is of the same order as the jet radius [see Fig. 5(b)]. Therefore the $m = 1$ optimal perturbation is expected to diffuse on a Re time scale. By contrast the optimal perturbations at higher m are azimuthally constrained and thus of smaller length scale [see Fig. 5(d)]. These perturbations are then expected to diffuse on a shorter time scale. To sum up, the $m = 1$ optimal perturbation benefits from a larger source of growth (high radial velocities in the jet shear layer), and during a larger time scale, than higher m perturbations. The optimal energy gain for $m = 1$ is therefore expected to be much larger than for higher m (it is noteworthy that hints of this behavior can be found in the non-modal global stability analysis of Garnaud *et al.*,[13] in which the authors notice that the largest growths are observed for $m = 1$ perturbations).

As mentioned earlier, Fig. 4 suggests exponential decays of G_{opt}/Re^2 and τ_{opt}/Re with m, for the range $m \geq 2$, with a steeper ratio in the case of optimal gains. Besides, it has also been shown (see Fig. 3) that there is an asymptotic behavior of G_{opt} and τ_{opt} with α, whose limit values are dependent on the azimuthal wavenumber m, i.e., as m grows, a thinner shear layer thickness (larger α) is required to obtain the largest G_{opt} and shortest τ_{opt}. After evaluation of results, it can be observed that $G_{opt} \propto 1/m^3$, as it is shown in Fig. 6, where we present the dependence on α/m of the rescaled maximum optimal gain and optimal time, i.e., $G_{opt} \cdot m^3$ for $Re = 10\,000$ [see Fig. 6(a)] and $G_{opt} \cdot m^3/Re^2$ for $Re = 10\,000$ and $100\,000$ [Fig. 6(b)]. It seems clear that, regardless of the Re number, curves of $G_{opt} \cdot m^3$ collapse for $m \geq 2$, while $m = 1$ is out of trend, highlighting again differences on the nature of mechanisms for $m = 1$, i.e., transient shift-up mechanism, and $m \geq 2$, a more classical lift-up effect, where vortices are concentrated along the shear layer. The collapse of curves is only achieved when the aspect ratio α is scaled with m, i.e., when the optimal perturbation wavelength is normalized by the shear layer characteristic length scale; proving that for a given jet profile, the largest optimal gain is achieved when both scales sort of couple. Regarding the optimal time, τ_{opt}, no clear exponential decay

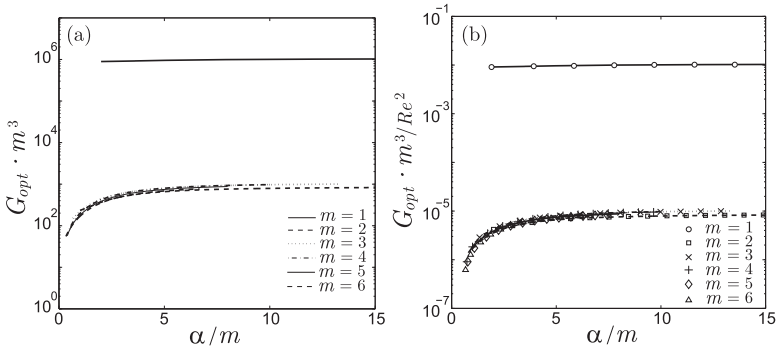

FIG. 6. Dependence on α/m of rescaled maximum optimal growth for a frozen base flow: (a) $G_{opt} \cdot m^3$, for $Re = 10\,000$, and (b) $G_{opt} \cdot m^3/Re^2$, for $Re = 10\,000$ (lines) and $100\,000$ (markers). For the sake of clarity, only curves corresponding $m = 1, 2, \ldots, 6$ are included in (b) for $Re = 100\,000$.

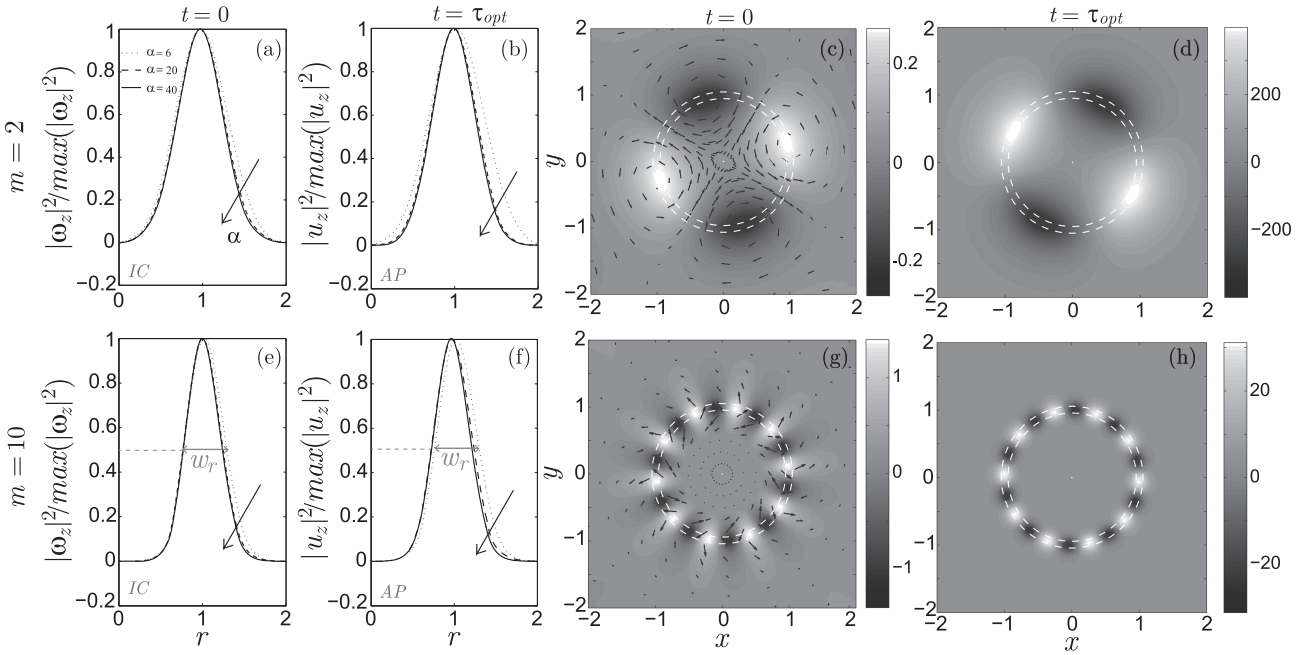

FIG. 7. Transient dynamics of optimal perturbations with $m = 2$ (top row) and $m = 10$ (bottom row) for frozen base flows at $Re = 100\,000$: [(a) and (e)] normalized axial components of enstrophy density $|\omega_z(r)|^2/\max(|\omega_z(r)|^2)$ at $t = 0$ and [(b) and (f)] energy density $|u_z(r)|^2/\max(|u_z(r)|^2)$ at optimal time $t = \tau_{opt}(\alpha)$ for different values of base flow aspect ratio α (arrows indicate sense of growing values, i.e., $\alpha = 6$: $\cdots$, $\alpha = 20$: - - -, and $\alpha = 40$: ——). For a base flow profile with $\alpha = 20$: [(c) and (g)] cross section of the optimal initial condition ($t = 0$) axial vorticity ω_z and associated normalized vector velocity field and [(d) and (h)] streamwise velocity u_z of the corresponding optimally amplified ($t = \tau_{opt}$) streaks. Dashed circles in (c), (d), (g), and (h) mark the limit of the shear layer, i.e., $r = 1 \pm 1/\alpha$, while gray tags in (e) and (f) define the radial width, w_r, of initial conditions (IC) and amplified perturbations (AP), plotted in Fig. 8.

trend has been found for the range of azimuthal wavenumbers investigated, although some approximations such as $\tau_{opt} \propto 1/m^2$ and $\tau_{opt} \propto 1/m^{2.5}$ have been tried (some results are included in Appendix B).

To evaluate in depth the effect of α and m on the structure of the optimal initial condition and most amplified streak, we further study the transient dynamics of optimal perturbations with $m = 2$ and $m = 10$ for $Re = 100\,000$ with the help of Fig. 7. Radial distributions of axial components of normalized perturbation enstrophy density, $|\omega_z|^2/\max(|\omega_z|^2)$, at initial time $t = 0$, and normalized perturbation kinetic energy, $|u_z|^2/\max(|u_z|^2)$, at optimal time $t = \tau_{opt}$, are, respectively, depicted in Figs. 7(a), 7(e), 7(b), and 7(f), for different values of $\alpha = 6$, 20, and 40. These distributions correspond, respectively, to streamwise vortices at initial time, and axial velocity streaks at optimal time, as the contours of axial vorticity [Figs. 7(c) and 7(g)] and axial velocity [Figs. 7(d) and 7(h)] show for $\alpha = 20$. It is noteworthy the fact that, regardless of the value of α, the enstrophy and energy density distributions barely collapse in single curves, which peak in the shear layer and extend radially approximately from $r = 0.5$ to $r = 1.5$ (a slight shift of structures appears to occur as the shear layer thickness is larger). This independence of optimal initial vortices and final streaks radial extension with respect to α is more clearly observed in Fig. 8, where we plot, for $\alpha = 20$ and 40, the evolution with m of the radial width w_r defined as the thickness of distributions corresponding to medium values, i.e., 0.5, of normalized enstrophy and energy, for optimal initial condition (streamwise vortices), $w_{r,IC}$, and most amplified perturbations (velocity streaks), $w_{r,AP}$, whose graphical definition is presented in Fig. 7. There it is shown that for a given α, a larger perturbation azimuthal wavenumber compresses the vortices and streaks radially, showing an asymptotic behavior for largest values of m. As the optimal initial vortices size decreases [see Figs. 7(c) and 7(g)], the magnitude of the axial vorticity ω_z (and corresponding radial

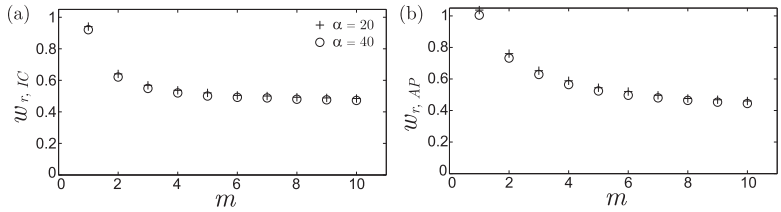

FIG. 8. Dependence on m of the radial width, w_r, of optimal initial conditions (streamwise vortices), i.e., $w_{r,IC}$, and most amplified perturbations (velocity streaks), $w_{r,AP}$, for $Re = 100\,000$ and $\alpha = 20$, 40. Widths $w_{r,IC}$ and $w_{r,AP}$ are defined, respectively, as the radial extension of normalized enstrophy and energy density distribution in Fig. 7, when $|\omega_z(r)|^2/\max(|\omega_z(r)|^2) = 0.5$ and $|u_z(r)|^2/\max(|u_z(r)|^2) = 0.5$. See Figs. 7(e) and 7(f) for graphic definition of variables.

velocity u_r) at initial time is larger, although the maximum axial velocity at optimal time features lower values than for perturbation with small m [see Figs. 7(d) and 7(h)], leading to lower energy gain. Consequently, the higher potential for transient growth at initial time for perturbations of large m seems to be hindered by the shorter perturbation diffusion time, which decreases with the azimuthal wavenumber, as shown in Fig. 4(b).

So far, the analysis has been done based on a jet velocity profile [Eq. (1)] which is considered to be steady, i.e., frozen in time. This assumption does not represent a major problem as long as the characteristic time of the perturbation evolution is much smaller that the diffusive time $\tau_D \simeq O(Re)$. However, as shown in Figs. 2 and 4(b), this is especially critical for low values of α and $m = 1$, for which $O(\tau_{opt}) \simeq O(Re)$. Consequently, if we want to force efficient optimal $m = 1$ perturbations in a round jet, for instance, with the aim at controlling Kelvin-Helmholtz instability, according to our previous results, we would have to wait a long temporal horizon τ_{opt} to obtain the maximum optimal growth G_{opt}, which would give the base flow enough time to diffuse, therefore rendering invalid the former analysis. Hence, the use of a diffusive jet velocity profile is required in the optimal perturbation analysis to draw realistic conclusions for $m = 1$ symmetries. However, the frozen base flow assumption should not pose a problem for optimal perturbations with $m \geq 2$, since $O(\tau_{opt}) \leq O(Re \cdot 10^{-1})$. Therefore, similar results are expected in those cases for analyzes based on frozen and diffusive base flows.

B. Diffusing base flow

We next discuss results obtained for the time evolution of optimal perturbations in a temporally diffusive base flow velocity profile, as defined in Eq. (A7). Figures 9(a) and 9(b) display, respectively, dependence with α of maximum optimal gain G_{opt} and optimal time τ_{opt}, for optimal perturbations of different azimuthal wavenumbers m at Reynolds number Re = 10 000 (note that only perturbations with $m \leq 6$ undergo transient growth at that value of Re). No major differences are found with respect to results included in Figs. 3(a) and 3(b) for a frozen base flow, with nearly identical asymptotic trends as α increases. However, the magnitudes of G_{opt} and τ_{opt} for m = 1 are clearly lower than those obtained for the frozen case. This shorter, and less energetic, transient dynamics for $m = 1$ perturbations evolving in a diffusing base flow is clearly observed in Figs. 9(c) and 9(d), where the dependence on m of rescaled optimal energy gain and optimal time, G_{opt}/Re^2 and τ_{opt}/Re, is presented for both frozen and diffusing base flows, with $\alpha = 20$ and $Re = 10\,000$. On one hand, it is observed that diffusion of base flow hinders the transient growth for perturbations with $m = 1$, whose energy gain is now virtually one third of that attained when the base flow is steady, while the optimal time decreases by a factor of 5 approximately. On the other hand, it seems evident that transient dynamics of optimal perturbations with $m \geq 2$ is less sensitive to base flow diffusion, which show values of G_{opt} and τ_{opt} that are not very different. For instance, for $m = 2$ when $\alpha = 20$ and $Re = 10\,000$, the frozen assumption provides with $G_{opt} \simeq 98.8$ and $\tau_{opt} \simeq 1248$, whereas $G_{opt} \simeq 85.8$ and $\tau_{opt} \simeq 967.5$ for a diffusing base flow. These results were anticipated, since the characteristic perturbation optimal times for $m \geq 2$ were, at least, one order of magnitude lower than the diffusing time scale for the base flow, i.e., $\tau_D \sim O(Re)$ [see Figs. 4(b) and 9(d)].[47] Besides, as occurred for the steady frozen base flow, the exponential decay with m showed by the optimal gain in Fig. 9(c) can be also properly rescaled using the law $G_{opt} \propto Re^2/m^3$, as depicted in Fig. 10, where results for $Re = 10\,000$, $100\,000$ and $m = 1, 2, \ldots, 6$, are included. As earlier, the scaling applies satisfactorily for $m \geq 2$. Thus, present results render valid, in general lines, the optimal perturbation analysis included in Sec. III A for perturbations with $m \geq 2$, although important quantitative differences are encountered for $m = 1$.

In order to understand how base flow diffusion affects the transient mechanism and structure of optimal initial vortices and most amplified streaks, we present in Fig. 11, for $m = 1$ and $m = 2$ perturbations, contours of axial vorticity ω_z and the associated velocity field at initial time $t = 0$ [Figs. 11(c) and 11(g)] and contours of axial velocity at terminal time $t = \tau_{opt}$ [Figs. 11(d) and 11(h)], for a diffusing base flow ($\alpha = 20$ and $Re = 1000$), whose time evolution is included in Figs. 11(a)–11(d), for both temporal horizons. In general, optimal initial vortices and optimal streaks are similar to those depicted in Fig. 5, although base flow diffusion gives rise to a radial spreading and smoothing of structures, both at initial and optimal times. When the evolution of the base flow is analyzed, it is seen that for $t = \tau_{opt}(m = 1)$, the jet core velocity is halved and the shear layer has vanished. The outcome of such process is an amplified perturbation with weaker and smoother

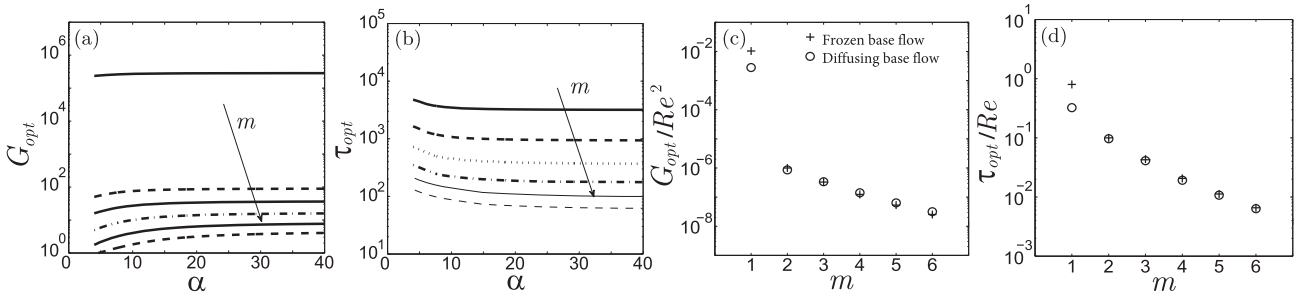

FIG. 9. Diffusing base flow at $Re = 10\,000$: dependence on α of (a) maximum optimal growth $G_{\max}$ and (b) optimal time τ_{opt}, for different values of azimuthal wavenumber, i.e., $m = 1, 2, \ldots, 6$ (arrows indicate growing values of m). Comparative between frozen and diffusing base flows with $\alpha = 20$ and $Re = 10\,000$: dependence on m of (c) G_{opt}/Re^2 and (d) τ_{opt}/Re.

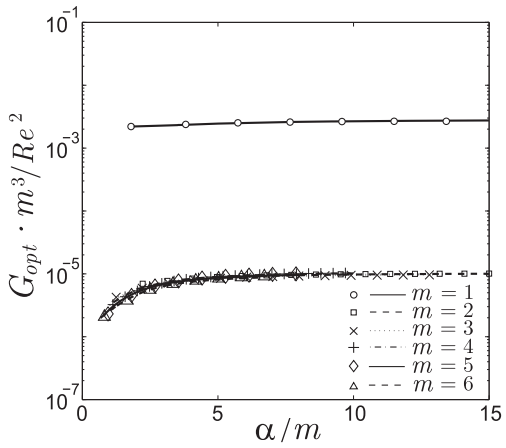

FIG. 10. Dependence on α/m of rescaled maximum optimal growth for a diffusing base flow, $G_{opt} \cdot m^3/Re^2$, for $Re = 10\,000$ (lines) and $100\,000$ (markers). For the sake of clarity, only curves corresponding $m = 1, 2, \ldots, 6$ are included for $Re = 100\,000$.

streaks of velocity [see Figs. 11(d) and 5(c) for comparison], although the magnitude of the initial axial vorticity is slightly bigger for the case at hand. Similarly, at $t = \tau_{opt}(m = 2)$, the shear layer has diffused in the jet profile, although the core velocity is almost unaffected. Consequently, the level of energy extracted now from the base flow is only slightly smaller than that transferred by the mechanism on a frozen flow, even if the magnitude of axial velocity [Fig. 11(h)] is clearly lower.

To analyze in depth differences in the energy transfer process, we display in Fig. 12 energy density distributions of optimal perturbations with $m = 1$ and $m = 2$, for frozen and diffusing base flows with $\alpha = 20$ at $Re = 1000$. More precisely, radial distributions of energy density components, $|u_i(r)|^2$ ($i = r, \theta, z$), are plotted at initial and optimal times, along with cross section contours of total energy density, $|u_r(r,\theta)|^2 + |u_\theta(r,\theta)|^2 + |u_z(r,\theta)|^2$, at $t = \tau_{opt}$ for most amplified perturbations. First, plots of radial distributions at initial and final times evidence the strong component-wise non-normality[45] that characterizes the lift-up (and shift-up) process, whereby the optimal initial forcing concentrates on radial and azimuthal components, while for the optimal response the axial component dominates. Interestingly, this component-wise non-normality is weakened by the base flow diffusion, especially for the optimal $m = 1$ perturbation, which renders the transient mechanism less efficient. Besides, the effect of vanishing shear is also observed at optimal time for both azimuthal wavenumbers. In fact, distributions of energy density attain sharper maxima at the shear layer ($r = 1$) when a frozen base flow is used [see Figs. 12(e), 12(f), 12(k), and 12(l)], since, as mentioned earlier, the location of streaks is mainly governed by the magnitude $-u_r dU/dr$, in the inviscid limit. However, when the base flow diffuses, the value of axial energy density varies smoothly around $r = 1$ [Figs. 12(b), 12(c), 12(h), and 12(i)], and optimal streaks spread over a larger radial extension. Consequently, the lower magnitudes of total energy density obtained for diffusing base flows [Figs. 12(c) and 12(i)] are partially compensated by the integration over a wider structure, providing with energy gains which are not very far from values achieved using a frozen profile, especially in the case of $m \geq 2$ (note that even for $m = 1$, gains in diffusing flows are always of the same order of magnitude that their frozen counterparts).

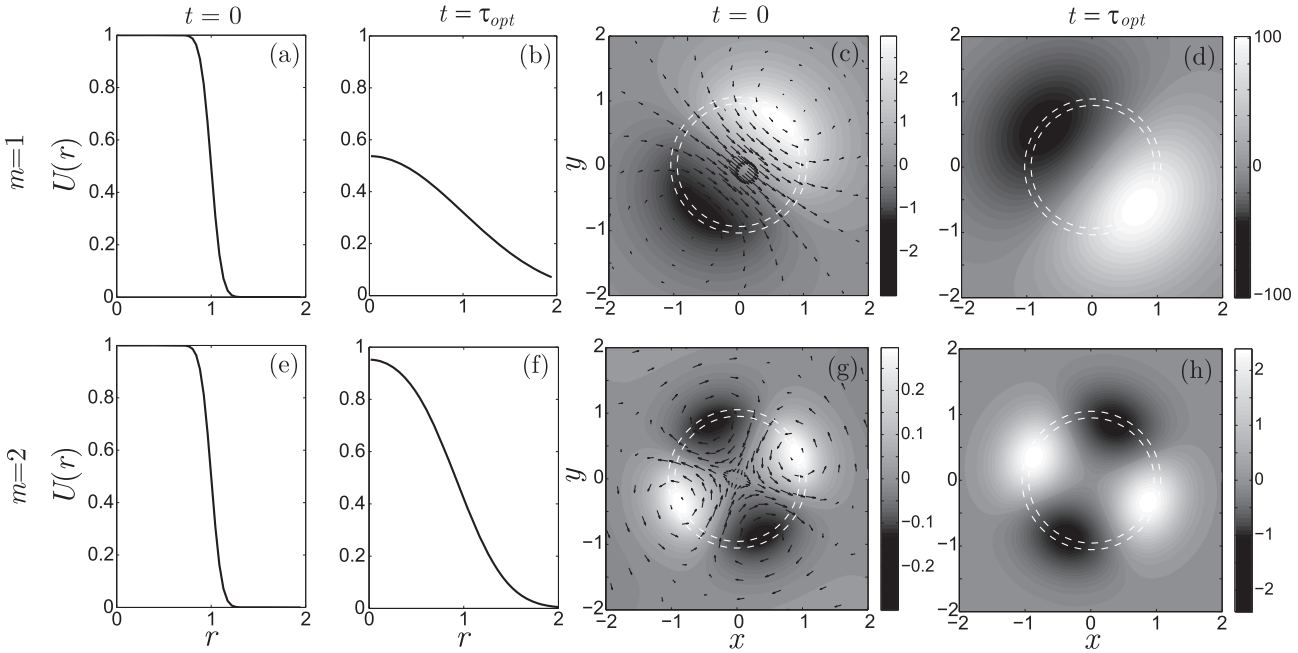

FIG. 11. Transient dynamics of perturbations for a diffusing base flow with $\alpha = 20$ and $Re = 1000$: cross section of the optimal initial condition ($t = 0$) axial vorticity ω_z and associated normalized vector field [(c) and (g)] and streamwise velocity u_z of the corresponding optimally amplified ($\tau = \tau_{opt}$) streak [(d) and (h)], for $m = 1$ [(a)-(d)] and $m = 2$ perturbations [(e)-(h)]. Dashed circles stand for the limit of the shear layer, i.e., $r = 1 \pm 1/\alpha$. Diffusion of base flow velocity profile $U(r)$ is also depicted at initial time [(a) and (e)] and optimal times [(b) and (f)].

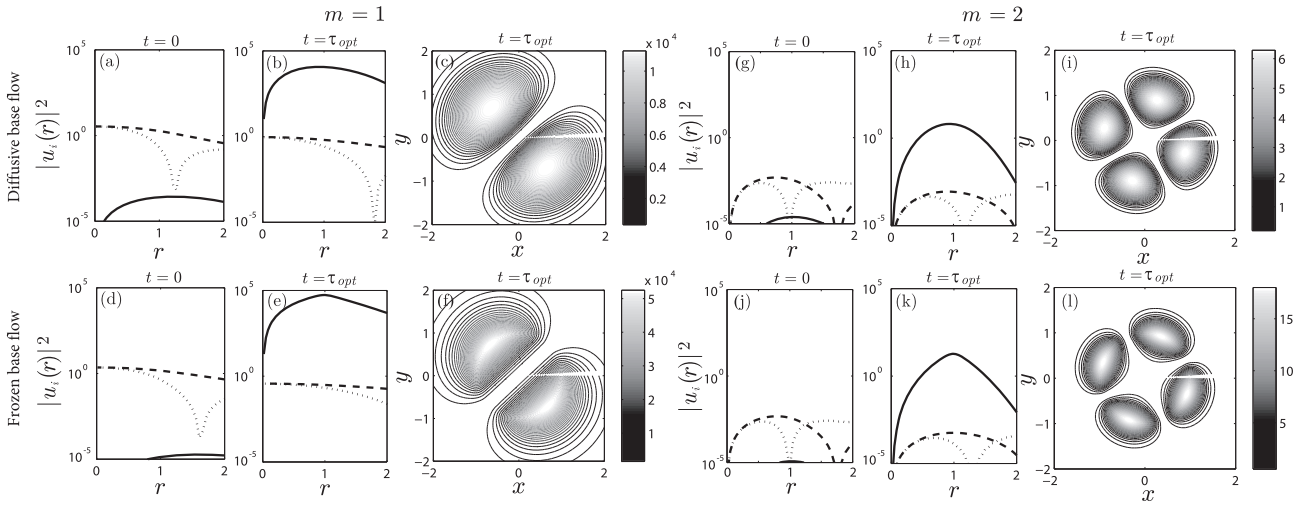

FIG. 12. Energy density distributions for optimal perturbations with $m = 1$ [(a)-(f)] and $m = 2$ [(g)-(l)] for diffusive (top row) and frozen (bottom row) base flows with $\alpha = 20$ at $Re = 1000$: radial energy densities $|u_i(r)|^2$ at (a), (d), (g), and (j) initial $t = 0$ and (b), (e), (h), and (k) optimal $t = \tau$ times ($|u_z(r)|^2$: thick solid lines, $|u_r(r)|^2$: dashed lines, and $|u_\theta(r)|^2$: dotted lines), and cross-sectional energy distribution $|u_r(r,\theta)|^2 + |u_\theta(r,\theta)|^2 + |u_z(r,\theta)|^2$ of the most amplified perturbations at optimal time $t = \tau$ [(c), (f), (i), and (l)].

IV. CONCLUSIONS

The potential for transient growth of streamwise invariant perturbations (axial wavenumber $k = 0$) in parallel round jets has been evaluated by means of an optimal perturbation analysis. In particular, the present study focuses on the transient evolution of three-dimensional disturbances with azimuthal wavenumbers $m \geq 1$, for different Reynolds numbers Re. Two types of analyses have been performed, concerning steady (frozen) and unsteady base flow velocity profiles of varying aspect ratio, $\alpha = R/\theta$, with the aim at evaluating the effect of base flow diffusion on the energy gain and dynamics of perturbations. Transient growth mechanisms have been characterized and discussed.

The first part of the study focused on steady base flow profiles, showing that for given values of Re and m, the transient dynamics is more energetic and shorter as the velocity profile steepens, i.e., increasing α. The dynamics can be characterized by a maximum optimal value of the energy gain, G_{opt}, attained at an optimal time, τ_{opt}, from which perturbation amplification decays. Therefore, steeper profiles provide with larger magnitudes of G_{opt} and shorter times τ_{opt}, both reaching asymptotic values in the limit of large α. As expected, when the Re is increased, the number of perturbations azimuthal wavenumbers, m, undergoing transient growth increases. In particular, $m = 1$ perturbations always display larger values of G_{opt} (four orders of magnitude) than $m \geq 2$; but they also require larger times τ_{opt} (at least one order of magnitude) to reach such energy gains. As observed in other unbounded shear flows,[27] G_{opt} and τ_{opt} grow with Re, retrieving the classical scaling laws: $G_{opt} \propto Re^2$ and $\tau_{opt} \propto Re$. Besides, the aforementioned asymptotic limits of optimal gains and times are attained at larger aspect ratios for growing m, which suggests that thinner shear layers are needed for shorter azimuthal wavelengths to transfer energy optimally from the jet to the perturbation in the transient. Interestingly, rescaled gains and times, G_{opt}/Re^2 and τ_{opt}/Re, decrease exponentially with m in the range $m \geq 2$ (Fig. 4), with $m = 1$ perturbations out of trends, suggesting qualitative differences between transient mechanisms for $m = 1$ and $m \geq 2$. After observation of results, we proposed the scaling law $G_{opt} \propto Re^2/m^3$, which makes curves of $G_{opt} \cdot m^3/Re^2$ collapse for $m \geq 2$ (Fig. 6). This collapse is only achieved if the characteristic perturbation wavelength is rescaled by the shear layer length scale, i.e., α/m, inferring that there is a coupling between scales in optimal transient dynamics. Again, $m = 1$ perturbations do not follow such trend, which may be based on differences on the nature of transient mechanisms.

An analysis of perturbations structure unveiled that optimal initial conditions correspond to streamwise counterrotating vortices, whereas the optimally amplified disturbances are axial velocity streaks, for all m investigated, although their radial extension and magnitude depend on the azimuthal wavenumber (Figs. 5 and 7). More precisely, for $m = 1$ perturbations, the shift-up effect[18] is observed: the dipole formed by the initial vortices induces a nearly uniform velocity flow in the jet core, which shifts the whole jet radially, giving rise to optimal axial velocity streaks at $t = \tau_{opt}$ which spread from the shear layer towards the jet core. Differently, optimal perturbations with higher values of m, i.e., $m \geq 2$, are more concentrated along the shear layer, in a way that resembles the classical lift-up mechanism, and feature lower values of vorticity. The latter induces a weaker cross-sectional radial flow, which hinders the value of G_{opt} and, therefore, the magnitude of axial streaks at $t = \tau_{opt}$, which are now located in the shear layer. Radial extension of optimal initial conditions and amplified responses is further investigated by means of radial distributions of axial enstrophy and kinetic energy, respectively (Figs. 7 and 8). It is observed that structures peak at the shear layer and extends radially a distance that is virtually the same regardless of the value of the jet aspect ratio, α. Besides, larger perturbation azimuthal wavenumbers compress the initial vortices and response streaks radially.

The first analysis, presented in Sec. III A, involved steady base flows, which do not represent a major drawback as long

as the diffusion time, $\tau_D \sim O(Re)$, is larger than the perturbation characteristic time scale. In view of results, for $m \geq 2$ this assumption is not unreasonable, since $O(\tau_{opt}) \leq O(Re \cdot 10^{-1})$, but it turns out to be too strong in the case of $m = 1$ perturbations, for which $O(\tau_{opt}) \simeq O(Re)$. Consequently, the use of a diffusing velocity profile was required to obtain realistic transient dynamics for $m = 1$ perturbations. In that sense, it has been shown that for a given Re, similar asymptotic trends are found, for steady and unsteady base flows, with respect to G_{opt} and τ_{opt} as α grows (Fig. 9). However, magnitudes of optimal gain and time are clearly lower for $m = 1$ when the base flow diffuses: G_{opt} decreases by a factor of 3, whereas τ_{opt} is divided by five approximately. Also, as expected, the transient dynamics of perturbations with $m \geq 2$ remains virtually unaltered quantitatively, rendering acceptable the former frozen assumption. As earlier, previous scaling laws $G_{opt} \propto Re^2/m^3$ and $\tau_{opt} \propto Re$ apply satisfactorily, although perturbations with $m = 1$ are again out of trend.

Transient evolution of base flow and perturbations has been analyzed (Fig. 11) to identify the origin of differences of dynamics for $m = 1$ perturbations and similarities encountered for $m \geq 2$ in both types of base flows. In general, the large optimal times shed by $m = 1$ perturbations lead to a strong diffusion of the base flow velocity profile, whereby the jet core velocity is halved and the shear layer vanishes. Consequently, the final streaks are now less concentrated around the shear layer, and feature weaker magnitudes. Conversely, the shorter time scale given by transient growth of $m \geq 2$ perturbations gives the base flow less time to diffuse, and now the jet core is barely unaffected. Thus, the level of energy extracted from the jet is only slightly smaller than in the case of frozen velocity profiles. Finally, a comparison between optimal perturbations evolving in frozen and diffusing base flows has been established (Fig. 12), by means of kinetic energy densities distributions. A strong component-wise non-normality has been identified, as a feature of the lift-up process, since the initial conditions mostly concentrated on radial and azimuthal components, while the optimal response is dominated by axial component. The base flow diffusion has been proven to undermine such non-normality and, therefore, the optimal response. Now, initial and amplified structures do not peak strongly in the shear layer but spread smoothly in the radial coordinate over a larger region. Integration of such wider area compensates slightly the weaker maximum energy magnitude of streaks, modulating the potential loss of energy gain with diffusion of base flow.

In general, the frozen analysis seems to provide acceptable results for perturbations with $m \geq 2$, although the use of diffusing base flows needs to be considered in the transient analysis of $m = 1$ disturbances. Altogether, the latter type of perturbations has a much higher potential for transient energy growth, guided by the shift-up mechanism, with leads to values of G_{opt} several order of magnitudes larger than those achieved by means of more three-dimensional perturbations, i.e., $m \geq 2$, whose transient dynamics is characterized by a more classical version of the lift-up effect. However, when time scale is compared, optimal times τ_{opt} are considerably shorter for $m \geq 2$ disturbances, which is interesting from the point of view of control, since it implies that optimal amplified perturbations can emerge very quickly in the flow, with a non-negligible energy gain even for initial conditions with large to moderate azimuthal wavenumbers m. This transient evolution could distort the flow, via nonlinear interactions, giving rise to a bypass scenario that hinders other unstable flow perturbations, such as those arising from the Kelvin-Helmholtz instability. Evaluation of real control potential using streamwise invariant optimal perturbations needs to be done employing nonlinear formulation or direct numerical simulations, which are considered a natural continuation of the present paper.

ACKNOWLEDGMENTS

This work has been financed by the Spanish MINECO (Subdirección General de Gestión de Ayudas a la Investigación) and Universidad de Jaén under Project Nos. DPI2014-59292-C3-03 and UJA2015/06/14, respectively. J.I.J.G. is also grateful to the Institut National Polytechnique de Toulouse for its support through the "Visiting Professors 2016" Program.

APPENDIX A: DIFFUSING BASE FLOW

The diffusing base flow considered in the present study is an axisymmetric parallel jet flow whose velocity profile is of the form $\mathbf{U} = U(r,t)\,\mathbf{e}_z$ in cylindrical coordinates (r,ϕ,z). The velocity profile U is built from the solution of the diffusion problem of an initial top-hat jet of radius R_0 and velocity U_0,

$$V(r,t) = \frac{U_0}{2\nu t}\exp\left(-\frac{r^2}{4\nu t}\right)\int_{s=0}^{R_0} s\exp\left(-\frac{s^2}{4\nu t}\right) I_0\left(\frac{sr}{2\nu t}\right) ds, \tag{A1}$$

where ν is the fluid kinematic viscosity and I_0 is the modified Bessel function of the first kind of order zero. The derivation of this solution can be found in the work of Osizik[46] (see Examples 3-6, pp. 122–124 in Sec. III C), where the equivalent heat conduction problem is solved by the method of separation of variables in the cylindrical coordinate system, via the use of integrals of Bessel functions.

We use this solution at a given time t_i to get the initial base flow profile

$$U(r,t=0) = V(r,t_i) = \frac{U_0}{2\nu t_i}\exp\left(-\frac{r^2}{4\nu t_i}\right) \times \int_{s=0}^{R_0} s\exp\left(-\frac{s^2}{4\nu t_i}\right) I_0\left(\frac{sr}{2\nu t_i}\right) ds. \tag{A2}$$

Velocity profiles for different times t_i are displayed in Fig. 13(a). The time evolution of this initial base flow profile is then given by

$$U(r,t\geq 0) = \frac{U_0}{2\nu(t_i+t)}\exp\left(-\frac{r^2}{4\nu(t_i+t)}\right) \times \int_{s=0}^{R_0} s\exp\left(-\frac{s^2}{4\nu(t_i+t)}\right) I_0\left(\frac{sr}{2\nu(t_i+t)}\right) ds. \tag{A3}$$

This velocity profile can be nondimensionalized by choosing a characteristic velocity scale U_j and a characteristic length

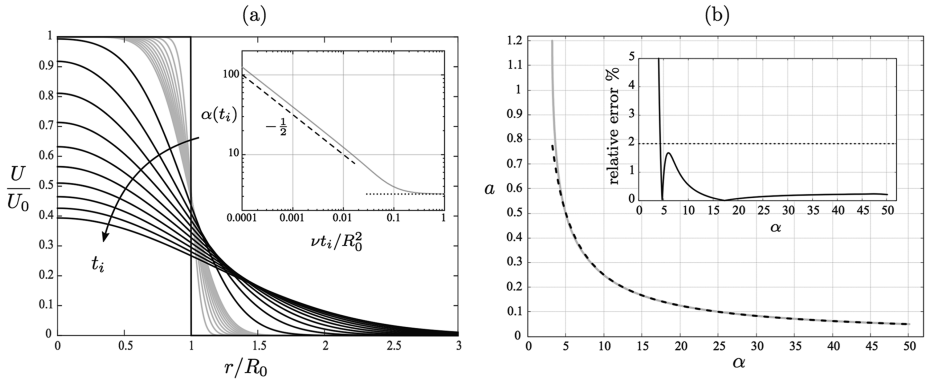

FIG. 13. (a) Time evolution of the velocity profile of an initial top-hat jet, for $\nu t_i/R_0^2$ from 0.002 to 0.02 in increments of 0.002 (gray lines) and from 0.05 to 0.5 in increments of 0.05 (black lines). The time evolution of the aspect ratio $\alpha(t_i)$ is displayed in the inset (solid line). The dashed line indicates the diffusion scaling law in $1/\sqrt{t_i}$, and the dotted line marks the theoretical asymptotic value for a Gaussian profile in the limit of large times. (b) Relationship between the initial base flow parameter a and the aspect ratio of the jet $\alpha = R_j/\theta$. The gray solid line corresponds to the numerical computation of the aspect ratio α for values of a between 0.5 and 1.2. The black dotted line corresponds to the approximation $a = 2.5/\alpha$, which is a good fit for $\alpha > 4.36$ (or $a < 0.585$, equivalently) with a relative error smaller than 2% (see the inset).

scale R: $U = U^\star U_j$, $r = r^\star R$, $s = s^\star R$, and then $t = t^\star R/U_j$. Dropping the star *, the base flow profile reads

$$U(r,t) = \frac{2\,U_0/U_j}{a^2 + 4t/Re}\exp\left(-\frac{r^2}{a^2+4t/Re}\right) \times \int_{s=0}^{R_0/R} s\exp\left(-\frac{s^2}{a^2+4t/Re}\right) I_0\left(\frac{2sr}{a^2+4t/Re}\right) ds, \tag{A4}$$

where $Re = U_j R/\nu$ is the Reynolds number and $a = \sqrt{4\nu t_i}/R$ is of the same order of magnitude as the nondimensional momentum thickness of the base flow profile shear layer at initial time.

Let U_j be defined as the jet velocity on the axis $r = 0$ at initial time. This implies that $U(r = 0,\, t = 0) = 1$ and since $I_0(0) = 1$, Eq. (A4) reduces to

$$1 = \frac{2\,U_0/U_j}{a^2}\int_{s=0}^{R_0/R} s\exp\left(-\frac{s^2}{a^2}\right) ds \tag{A5}$$

or, equivalently,

$$U_0/U_j = \left[1 - \exp\left(-\frac{R_0^2}{R^2a^2}\right)\right]^{-1}. \tag{A6}$$

Then the nondimensional base flow profile is given by

$$U(r,t) = \frac{2\exp\left(-\frac{r^2}{a^2+4t/Re}\right)}{\left(a^2+4t/Re\right)\left[1-\exp\left(-\frac{R_0^2}{R^2a^2}\right)\right]} \times \int_{s=0}^{R_0/R} s\exp\left(-\frac{s^2}{a^2+4t/Re}\right) I_0\left(\frac{2sr}{a^2+4t/Re}\right) ds. \tag{A7}$$

Finally let R be defined as the radius at which the initial velocity profile corresponds to half the (maximum) velocity on the axis. This implies that $U(r = 1,\, t = 0) = 1/2$ and Eq. (A7) writes

$$\frac{1}{2} = \frac{2\exp\left(-\frac{1}{a^2}\right)}{a^2\left[1-\exp\left(-\frac{R_0^2}{R^2a^2}\right)\right]}\int_{s=0}^{R_0/R} s\exp\left(-\frac{s^2}{a^2}\right) I_0\left(\frac{2s}{a^2}\right) ds \tag{A8}$$

and the unknown $X = R_0/R$ is solution of the following integral equation:

$$\int_{s=0}^{X} s\exp\left(-\frac{s^2}{a^2}\right) I_0\left(\frac{2s}{a^2}\right) ds = \frac{a^2}{4}\exp\left(\frac{1}{a^2}\right)\left[1-\exp\left(-\frac{X^2}{a^2}\right)\right]. \tag{A9}$$

Once Eq. (A9) is solved, the diffusing base flow profile given by Eq. (A7) depends only on two non-dimensional parameters, namely, the Reynolds number Re and the shape factor a which can be related to the momentum thickness of the velocity profile and therefore to the aspect ratio $\alpha = R/\theta$ of the jet. Figure 13(b) displays the relationship between a and α that can be computed from the velocity profile given in Eq. (A7). An approximate analytical relationship $\alpha = 2.5/a$ can be deduced from these numerical results, with a relative error of less than 2%.

APPENDIX B: DEPENDENCE ON m OF τ_{opt}/Re

As shown in Sec. III, the optimal time τ_{opt} apparently decays exponentially as the perturbation azimuthal wavenumber m increases. Unlike the maximum optimal gain G_{opt}, for which the scaling law $G_{opt} \propto Re^2/m^3$ applies satisfactorily, for both frozen and diffusing base flow (see Figs. 6 and 10), τ_{opt} does not seem to follow a unique scaling law in the whole range of m investigated. For instance, Fig. 14 shows different rescaled functions of optimal time, $\tau_{opt}\cdot m^2$ and $\tau_{opt}\cdot m^{2.5}$ for $Re = 10\,000$ and $\tau_{opt}\cdot m^2$ for $Re = 100\,000$, where it is seen that there is no collapse of all curves for any law used nor number of Re. In fact, it is seen that for $Re = 10\,000$, $\tau_{opt} \propto 1/m^{2.5}$ make curves overlap only for $m \geq 3$, while for $Re = 100\,000$, a fair collapsing is achieved for $m \geq 6$ employing $\tau_{opt} \propto 1/m^2$.

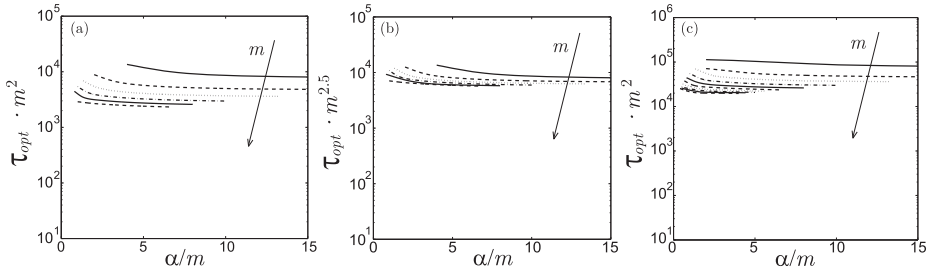

FIG. 14. Dependence on α/m of optimal time for a frozen base flow: (a) $\tau_{opt} \cdot m^2$ ($Re = 10\,000$), (b) $\tau_{opt} \cdot m^{2.5}$ ($Re = 10\,000$), and (c) $\tau_{opt} \cdot m^2$ ($Re = 100\,000$).

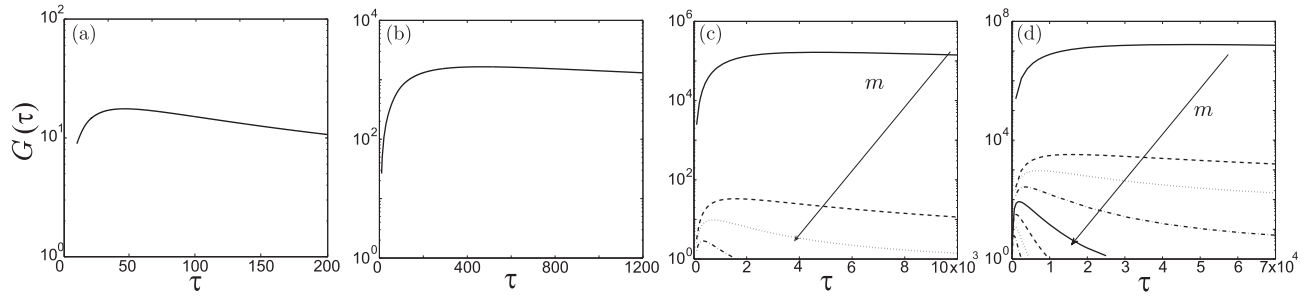

FIG. 15. Diffusing Gaussian base flow: evolution of energy gain $G(\tau)$ with the optimal terminal time τ, for (a) $Re = 100$, (b) $Re = 1000$, (c) $Re = 10\,000$, and (d) $Re = 100\,000$. Arrows indicate sense of growing values of m.

In view of such results, no exponential law has been proposed in the manuscript.

APPENDIX C: DIFFUSING GAUSSIAN BASE FLOW

To complete the study on canonical round jets profiles, we have performed a complementary optimal perturbation analysis of streamwise invariant disturbances evolving in a classical Gaussian velocity profile. This study aims at evaluating the potential for transient growth of streamwise vortices in the absence of strong flow shear. The optimal perturbation analysis has been performed for four selected Reynolds numbers, i.e., $Re = 100$, 1000, 10 000, and 100 000, employing the following unsteady jet velocity profile:

$$U(r,t) = \frac{1}{1+4t/Re} \exp[-r^2/(1+4t/Re)]. \qquad \text{(C1)}$$

Results obtained from such study are presented in Fig. 15, which displays the curves of energy gain $G(\tau)$ versus the temporal horizon τ, for optimal perturbations of different azimuthal wavenumber m, and selected values of Reynolds number. Evaluation of figures evidences the stabilizing effect of a fully developed profile in terms of m, when compared to the base flow defined in Eq. (A7), since, for a given Re, there are fewer values of perturbation azimuthal wavenumber m that undergo transient growth [see Fig. 9(a) for comparison]. Note that at $Re = 1000$ only energy of optimal $m = 1$ perturbations grows transiently, while at $Re = 10\,000$ this transient amplification is limited to optimal perturbations with $m \leq 4$. This effect of vanishing shear layer was also especially remarkable at low values of jet profile aspect ratio α in Fig. 9(a). Besides, for every Re and m investigated, curves of $G(\tau)$ present a quick growth at low values of τ, until reaching the maximum optimal gain $G_{opt} = sup_\tau(G(\tau))$ at an optimal time τ_{opt}, from where the gain decays monotonically. This decay rate becomes faster as the perturbation azimuthal wavenumber increases, in such a way that for largest values of m transient growth is limited, as expected, to very short times. As seen in Fig. 16, where dependence on m of rescaled G_{opt}/Re^2 and τ_{opt}/Re is displayed, trends resemble those obtained in Sec. III B for low values of α. Again, optimal $m = 1$ perturbations attain

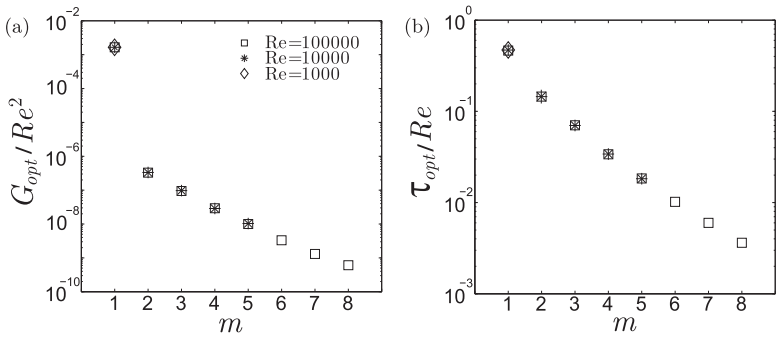

FIG. 16. Diffusing Gaussian base flow: (a) G_{opt}/Re^2 and (b) τ_{opt}/Re dependence on the azimuthal wavenumber m.

values of G_{opt} which are three orders of magnitude larger than the corresponding gain for $m = 2$, but in general, the transient dynamics of perturbations in a Gaussian jet, i.e., a fully developed profile, is less efficient, being it characterized by a weaker optimal gain G_{opt} and a longer optimal times τ_{opt} than that existing in top-hat profiles (large α). Finally, it must be highlighted that the scaling law $G_{opt} \propto 1/m^3$ that was used in Sec. III B does not apply here (similarly, it can be observed in Fig. 10 that the scaling law is better suited for intermediate and large values of α/m).

APPENDIX D: NUMERICAL CONVERGENCE

The optimization problem was solved using a pseudospectral Chebyshev technique,[18] where the infinite radial coordinate is first mapped onto a Chebyshev space, $s \in [-1, +1]$, using a Gauss-Lobatto grid of N points. This grid is adjusted so that $r \in \ ]-\infty, +\infty[$, taking afterwards only the positive semi-infinite grid, $r > 0$. The algebraic mapping used reads $r(s) = \gamma s/\sqrt{1-s^2}$, where γ is the stretching factor that controls the points spreading after imposing the radius of the penultimate point, $r_{\max}$, and that is defined as $\gamma = r_{\max}\sqrt{\left(1 - s_{2N+1}^2\right)}/s_{2N+1}$, being s_{2N+1} the penultimate point of the Gauss-Lobatto grid. Thus, the critical parameter to ensure accuracy of results and convergence corresponds to the number of points within the shear layer, whose value will depend on the total number of points, N, and on the maximum radius for the mapping, $r_{\max}$. Besides, to avoid problems of spectral instability and large computational times, a moderate value of N is advisable, which must be combined with a sufficiently large $r_{\max}$, to map properly the slow algebraic decay of perturbations with r (see Fig. 12 in Ref. 18).

Table I presents results of optimal gain $G(\tau)$ at given optimal times τ, for the steepest base flow profile investigated, i.e., $\alpha = 40$, and therefore the largest shear, at $Re = 100\,000$. Tests of optimal perturbations with $m = 1$ using frozen and diffusing base flows are listed, along with corresponding computational times (using processors Intel®Core i7-5600U 2.60 GHz). In view of the results, the energy gain $G(\tau)$ may vary substantially depending on the set of parameters $(r_{\max}, N)$ selected. Therefore, we consider that convergence is achieved when $G(\tau)$ yields the same value with six significant digits. In that sense, in order to obtain a converged value of $G(\tau)$, the analysis requires to employ a minimum mapping radius, e.g., $r_{\max} \geq 100$, in combination with enough points N to describe the shear layer. This can be also noticed in Fig. 17, where the base flow profile, $U(r)$, and the axial component of enstrophy density for the optimal initial condition, $|\omega_z(r)|^2$, are plotted for four different pairs of values $(r_{\max}, N)$, namely, (50, 50), (150, 100), (150, 150), and (300, 200). It seems evident that for $(r_{\max}, N) = (50, 50)$, the shear layer is not adequately mapped, which, combined with the fair radial extension covered, gives rise to an optimal initial condition which is not well defined. As $r_{\max}$ and N increase accordingly, the shear layer is better resolved and the optimal initial condition evolves towards a converged shape. Note that for $(r_{\max}, N) = (150, 150)$ and $(r_{\max}, N) = (300, 200)$, base flow profiles and enstrophy densities nearly overlap. This convergence behavior is also found when a diffusing base flow is used. Therefore, taking into account these results and evaluating the computational time requirements (especially demanding when diffusing base flows are considered), we choose $N = 150$ and $r_{\max} = 150$ as the best compromise solution between accuracy and feasibility. Hence, all results presented in this work have been obtained using this set of parameter.

TABLE I. Convergence study of optimal $m = 1$ perturbations for frozen (Fr) and diffusive (Di) base flows with $\alpha = 40$, at $Re = 100\,000$.

Type	τ	$r_{\max}$	N	$G(\tau)$	*Time* (s)
Fr	80 000	50	50	$1.067\,09\times10^{8}$	3.8829
Fr	80 000	50	100	$1.039\,10\times10^{8}$	4.7121
Fr	80 000	100	50	$6.990\,71\times10^{7}$	4.1671
Fr	80 000	100	100	$1.038\,05\times10^{8}$	4.6253
Fr	80 000	150	100	$1.037\,84\times10^{8}$	4.6416
Fr	80 000	150	150	$1.038\,03\times10^{8}$	8.2792
Fr	80 000	150	300	$1.038\,03\times10^{8}$	36.7455
Fr	80 000	300	200	$1.038\,03\times10^{8}$	16.9419
Di	32 000	150	100	$2.840\,89\times10^{7}$	1 012.1619
Di	32 000	150	150	$2.840\,91\times10^{7}$	3 921.1145
Di	32 000	300	200	$2.840\,91\times10^{7}$	12 740.2497

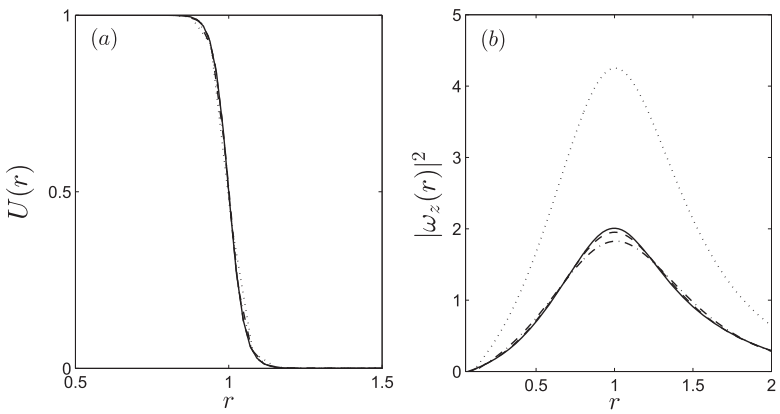

FIG. 17. Convergence study for optimal $m = 1$ perturbations using a frozen base flow with $\alpha = 40$ and $Re = 100\,000$: (a) details of the shear layer in the base flow profile $U(r)$ and (b) axial component of enstrophy density for the optimal initial condition, $|\omega_z(r)|^2$. Four different sets of $(r_{\max}, N)$ are plotted for comparison, i.e., $(50, 50)$: $\cdots$, $(150,100)$: - · -, $(150, 150)$: – – –, and $(300, 200)$: ——.

[1]G. K. Batchelor and E. Gill, "Analysis of the stability of axisymmetric jets," J. Fluid Mech. **14**, 529–551 (1962).
[2]A. Michalke, "On the inviscid instability of the hyperbolic-tangent velocity profile," J. Fluid Mech. **19**(4), 543–556 (1964).
[3]D. G. Crighton and M. Gaster, "Stability of slowly diverging jet flow," J. Fluid Mech. **77**(2), 397–413 (1976).
[4]P. J. Morris, "The spatial viscous instability of axisymmetric jets," J. Fluid Mech. **77**, 511–529 (1976).
[5]A. Michalke and G. Hermann, "On the inviscid instability of a circular jet with external flow," J. Fluid Mech. **114**, 343–359 (1982).
[6]A. Michalke, "Survey on jet instability theory," Prog. Aerosp. Sci. **21**, 159–199 (1984).
[7]M. Abid, M. Brachet, and P. Huerre, "Linear hydrodynamic instability of circular jets with thin shear layers," Eur. J. Mech., B: Fluids **12**(5), 683–693 (1993).
[8]M. P. Lessen and P. J. Singh, "The stability of axisymmetric free shear layers," J. Fluid Mech. **60**, 433–457 (1973).
[9]P. Plaschko, "Helical instabilities of slowly divergent jets," J. Fluid Mech. **92**(2), 209–215 (1979).
[10]P. J. Schmid and D. S. Henningson, *Stability and Transition in Shear Flows* (Springer-Verlag, 2001).
[11]T. Ellingsen and E. Palm, "Stability of linear flow," Phys. Fluids **18**(4), 487–488 (1975).
[12]M. T. Landahl, "A note on an algebraic instability of inviscid parallel shear flows," J. Fluid Mech. **98**(2), 243–251 (1980).
[13]X. Garnaud, L. Lesshafft, P. J. Schmid, and P. Huerre, "Modal and transient dynamics of jet flows," Phys. Fluids **25**, 044103 (2013).
[14]S. A. Boronin, J. J. Healey, and S. S. Sazhin, "Non-modal stability of round viscous jets," J. Fluid Mech. **716**, 96–119 (2013).
[15]L. Brandt, "The lift-up effect: The linear mechanism behind transition and turbulence in shear flows," Eur. J. Mech., B: Fluids **47**, 80–96 (2014).
[16]W. M. F. Orr, "The stability or instability of the steady motions of a perfect liquid and of viscous liquid. Part I: A perfect liquid," Proc. R. Ir. Acad., Sect. A **27**, 9–68 (1907–1909), available at http://www.jstor.org/stable/20490590; "The stability or instability of the steady motions of a perfect liquid and of a viscous liquid. Part II: A viscous liquid," *ibid*. **27**, 69–138 (1907–1909); available at http://www.jstor.org/stable/20490591.
[17]X. Garnaud, L. Lesshafft, P. J. Schmid, and P. Huerre, "The preferred mode of incompressible jets: Linear frequency response analysis," J. Fluid Mech. **716**, 189–202 (2013).
[18]J. I. Jiménez-González, P. Brancher, and C. Martínez-Bazán, "Modal and non-modal evolution of perturbations for parallel round jets," Phys. Fluids **27**, 044105-1–044105-19 (2015).
[19]Y. Detandt, "Numerical simulation of aerodynamic noise in low Mach number flows," Ph.D. thesis, Université Libre de Bruxelles, Belgium, 2007.
[20]T. H. New and W. L. Tay, "Effects of cross-stream radial injections on a round jet," J. Turbul. **7**, 1–20 (2006).
[21]M. B. Alkislar, A. Krothapalli, and G. W. Butler, "The effect of streamwise vortices on the aeroacoustics of a Mach 0.9 jet," J. Fluid Mech. **578**, 139–169 (2007).
[22]P. Zhang, "Active control of a turbulent round jet based on unsteady microjets," Ph.D. thesis, The Hong Kong Polytechnic University, 2014.
[23]H. Yang, Y. Zhou, R. M. C. So, and Y. Liu, "Turbulent jet manipulation using two unsteady azimuthally separated radial minijets," Proc. R. Soc. A **472**, 20160417 (2016).
[24]N. A. Bakas and P. J. Ioannou, "Modal and nonmodal growths of inviscid planar perturbations in shear flows with a free surface," Phys. Fluids **21**, 024102 (2009).
[25]C. Cossu and L. Brandt, "Stabilization of Tollmien-Schlichting waves by finite amplitude optimal streaks in the Blasius boundary layer," Phys. Fluids **14**(8), L57–L60 (2002).
[26]C. Cossu and L. Brandt, "On Tollmien–Schlichting-like waves in streaky boundary layers," Eur. J. Mech., B: Fluids **23**, 815–833 (2004).
[27]G. Del Guercio, C. Cossu, and G. Pujals, "Stabilizing effect of optimally amplified streaks in parallel wakes," J. Fluid Mech. **739**, 37–56 (2014).
[28]G. Del Guercio, C. Cossu, and G. Pujals, "Optimal streaks in the circular cylinder wake and suppression of the global instability," J. Fluid Mech. **752**, 572–588 (2014).
[29]G. Del Guercio, C. Cossu, and G. Pujals, "Optimal perturbations of non-parallel wakes and their stabilizing effect on the global instability," Phys. Fluids **26**, 024110-1–024110-14 (2014).
[30]M. Marant, C. Cossu, and G. Pujals, "Optimal streaks in the wake of a blunt-based axisymmetric bluff body and their influence on vortex shedding," C. R. Mec. **345**, 378–385 (2017).
[31]L. H. Gustavsson, "Energy growth of three-dimensional disturbances in plane Poiseuille flow," J. Fluid Mech. **224**, 241–260 (1991).
[32]S. S. Sazhin, S. B. Martynov, T. Kristyadi, C. Crua, and M. R. Heikal, "Diesel fuel spray penetration, heating, evaporation and ignition: Modeling versus experimentation," Int. J. Eng. Syst. Modell. Simul. **1**, 1–19 (2008).
[33]S. S. Sazhin, S. A. Boronin, S. Begg, C. Crua, J. Healey, N. A. Lebedeva, A. N. Osiptsov, F. Kaplanski, and M. R. Heikal, "Jet and vortex ring-like structures in internal combustion engines: Stability analysis and analytical solutions," Proc. IUTAM **8**, 196–204 (2013).
[34]P. Marmottant and E. Villermaux, "On spray formation," J. Fluid Mech. **498**, 73–111 (2004).
[35]A. Michalke, "Instabilität eines kompressiblen runden freistrahls unter berücksichtigung des einflusses der strahlgrenzschichtdicke," Z. Flugwiss. **8-9**, 319–328 (1971).
[36]P. Corbett and A. Bottaro, "Optimal linear growth in swept boundary layers," J. Fluid Mech. **435**, 1–23 (2001).
[37]A. Antkowiak and P. Brancher, "Transient energy growth for the Lamb-Oseen vortex," Phys. Fluids **16**(1), L1–L4 (2004).
[38]A. Antkowiak, "Dynamique aux temps courts d'un tourbillon isolé," Ph.D. thesis, Université Paul Sabatier de Toulouse, France, 2005.
[39]B. Fornberg, *A Practical Guide to Pseudospectral Methods* (Cambridge University Press, 1995).
[40]C. Canuto, M. Y. Hussaini, A. Quarteroni, and T. Zhang, *Spectral Methods in Fluid Dynamics* (Springer, 1988).
[41]J. A. C. Weideman and S. C. Reddy, "A MATLAB differentiation matrix suite," ACM Trans. Math. Software **26**(4), 465–519 (2000).
[42]R. R. Kerswell and A. Davey, "On the linear instability of elliptic pipe flow," J. Fluid Mech. **316**, 307–324 (1996).
[43]P. J. Schmid and D. S. Henningson, "Optimal energy density growth in Hagen-Poiseuille flow," J. Fluid Mech. **277**, 197–225 (1994).
[44]K. M. Butler and B. F. Farrell, "Three-dimensional optimal perturbations in viscous shear flow," Phys. Fluids A **4**(8), 1637–16509 (1992).
[45]J.-M. Chomaz, "Global instabilities in spatially developing flows: Non-normality and nonlinearity," Annu. Rev. Fluid Mech. **37**, 357–392 (2005).
[46]N. Osizik, *Heat Conduction*, 2nd ed. (John Wiley & Sons, 1993).
[47]As underlined by one referee, it should be noted that slightly larger growths are observed at $m > 3$ for the diffusing base flow, which is counter-intuitive. The diffusion of the base flow is associated with the diffusion of the jet momentum thickness and therefore a decrease of the aspect ratio α. As a first approximation, one could extrapolate the analysis done in the frozen case by applying these results to an effective aspect ratio, which is smaller than the initial one due to diffusion. In terms of energy gain, this approach would predict a wrong trend, namely, a lower growth, since the gain decreases for decreasing α [see Fig. 3(a)]. Nevertheless, it turns out that the optimal perturbation in the diffusing case has a radial extension which is larger than in the frozen case [data not shown for $m > 3$ but this trend is already visible for $m = 2$, see Figs. 12(i) and 12(l)]. As suggested by the referee, it is as if the optimal perturbation anticipates the diffusion of the shear layer and adapts itself with a wider spatial extent in order to resist better to its own viscous diffusion. As a consequence, the optimal perturbation is expected to be less affected by viscous diffusion than in the frozen case and therefore to better benefit from the energy growth mechanism at play in the shear layer, hence an eventual higher growth.